Journal of Alloys and Compounds 867 (2021) 158930

Contents lists available at ScienceDirect

Journal of Alloys and Compounds

journal homepage: www.elsevier.com/locate/jalcom

Enhanced yield synthesis of bulk dense $(M_{2/3}Y_{1/3})_2AlC$ (M = Cr, W, Mo) in-plane chemically ordered quaternary atomically laminated *i*-MAX phases and oxidation of $(Cr_{2/3}Y_{1/3})_2AlC$ and $(Mo_{2/3}Y_{1/3})_2AlC$

Tarek Ali ElMelegy[a], Maxim Sokol[a,b], Michel W. Barsoum[a,*]

[a] Drexel University, Department of Materials Science & Engineering, Philadelphia, PA, USA
[b] Department of Materials Science and Engineering, Tel Aviv University, Ramat Aviv 6997801, Israel

ARTICLE INFO

Article history:
Received 23 October 2020
Received in revised form 15 January 2021
Accepted 25 January 2021
Available online 29 January 2021

Keywords:
Chemical order
Synthesis
i-MAX phase
Oxidation
Ceramics
Transition metal alloys and compounds

ABSTRACT

Recently, a new family of MAX phases with in-plane chemical order, *i*-MAX, have been discovered which incorporate new elements expanding the family of MAX phases. *i*-MAX phases remain to be synthesized in single-phase bulk form for characterization. Herein, we show that by reactively hot pressing an intermetallic precursor, $Y_{2.23}Al$, instead of elemental Y, in combination with excess overall Al and a sub-stoichiometric fraction of carbon, we enhance the yield of $(Cr_{2/3}Y_{1/3})_2AlC$ to 85 ± 3 wt% (86 ± 3 mol%). Both the fractions of the impurity Y_2O_3 phase and the undesirable ternary Cr_2AlC are reduced. Subsequent isothermal oxidation of $(Cr_{2/3}Y_{1/3})_2AlC$ in natural air in the 1000–1400 °C temperature range reveals the formation of $Y_3Al_2(AlO_4)_3$ (YAG), Cr_2O_3 and Y_2O_3, without a continuous Cr_7C_3 sub-layer. Additionally, we show that by starting with $Y_{2.23}Al$ reagent we synthesize dense bulk $(W_{2/3}Y_{1/3})_2AlC$ and $(Mo_{2/3}Y_{1/3})_2AlC$ samples with enhanced *i*-MAX yields of 72 ± 3 wt% (59 ± 2 mol%) and 91 ± 3 wt% (72 ± 2 mol%), respectively. Oxidation of $(Mo_{2/3}Y_{1/3})_2AlC$ at 1300 °C for 12 h leads to formation of a thick, porous oxide of $Y_2Mo_3O_{12}$.

1. Introduction

Atomically laminated $M_{n+1}AX_n$ (MAX) phases - where M is an early transition metal, A is an A-group element (mostly Groups 13 and 14), X is C, N or B and n = 1 – 4 [1–4] - possess favorable properties hybrid between metallic and ceramic. A number of MAX phases (i.e. Ti_2AlC, Ti_3AlC_2, Cr_2AlC) possess good mechanical strength, damage tolerance, shock resistance, corrosion resistance (i.e. Cr_2AlC), and oxidation resistance [2].

Cr_2AlC specifically presents a good candidate for hot-corrosion resistance, oxidation resistance, erosion resistance and self-healing characteristics as well as low neutron absorption cross section [5–19]. These properties nominate Cr_2AlC phase for accident-tolerant fuel cladding used in light water reactors [20,21]. Cr_2AlC is a known alumina former with excellent isothermal and good cyclic oxidation resistance. However, a Cr_7C_3 carbide underlayer forms below the Al_2O_3 oxide scale which becomes problematic if the passivating Al_2O_3 layer is breached [13]. Moreover, challenges arise at higher temperatures (i.e. >1200 °C) due to possible scale spallation and wrinkling of the alumina scale [13,16]. Cr_2AlC is thus less resistant to cyclic oxidation above 1200 °C [19].

Oxide scale wrinkling phenomenon is recognized for other alumina forming materials [22–26]. There are two main theories explaining the formation of wrinkles; namely due to compressive stresses through lateral oxide growth within the grain boundaries [27], or due to the formation of a volatile gaseous phase which bubbles outside of the oxide scale. Wrinkling has been addressed in FeCrAl and other alloys through the addition of reactive elements (RE) (e.g. Hf, Y, Zr) which modifies oxide growth rate and improves scale adhesion and thus spallation resistance [22,28–33].

Oxidation improvement mechanism by RE additions is suggested to be due to: prevention of S impurity segregation at grain boundaries in the case of FeCrAl alloys, or segregation of reactive-element ions to the oxide scale grain boundaries and the metal-oxide interface [27,32,34–38]. It is argued that Y-doping in alumina-forming alloys (e.g. FeCrAl) transforms early oxidation mechanism into predominantly inward growth, and it is suggested that this promotes scale adhesion by avoiding the porous scale/alloy interface typical for outward grown scales [39]. Furthermore, Y additions can improve the high-temperature steam tolerance of FeCrAl alloys [40,41]. For the Cr_2AlC MAX phase, Y-doping has been shown to promote favorable oxidation behavior, improve oxide scale adherence and

* Corresponding author.
E-mail address: barsoumw@drexel.edu (M.W. Barsoum).

https://doi.org/10.1016/j.jallcom.2021.158930
0925-8388/

Table 1
Specifications for reagent powders used herein for $(M_{2/3}Y_{1/3})_2AlC$ *i*-MAX synthesis.

Reagent	Supplier	Purity (metals basis wt%)	Particle size (μm)	Mesh size #
Cr	Alfa Aesar, Kandel, Germany	99%	<45	−325
W	Alfa Aesar, Kandel, Germany	99.9%	<45	−325
Mo	Alfa Aesar, Kandel, Germany	99.9%	~58	−250
Al	Alfa Aesar, Kandel, Germany	99.5%	<45	−325
Y/Al (88/12 wt%) (~$Y_{2.23}Al$)	PLANSEE, Lechbruck, Germany	99.4%	<45	~325
C	Alfa Aesar, Kandel, Germany	99%, crystalline	<37	−300

affect oxide scale morphology and growth [42–44]. This supports the idea that doping some alumina-forming MAX phases (e.g. Cr_2AlC) with Y element could enhance oxidation resistance and high-temperature steam tolerance in similitude to FeCrAl alloys [22,28–33].

In a relevant attempt to introduce secondary elements in MAX phases, recently, in-plane chemically ordered quaternary *i*-MAX phases $(Mo_{2/3}Sc_{1/3})_2AlC$, $(Mo_{2/3}Y_{1/3})_2AlC$, $(V_{2/3}Zr_{1/3})_2AlC$ have been both predicted and synthesized from elemental precursors [45,46]. The chemical ordering in the case of *i*-MAX is within the M layers. They are reported to crystallize in both C2/c monoclinic and/or Cmcm orthorhombic space groups. An attempt to take advantage of Zr small neutron absorption cross-section was made through synthesis of $(Cr_{2/3}Zr_{1/3})_2AlC$ by Chen et. al [47]. Samples were sintered using ZrH_2 precursor instead of elemental Zr [47]. Chen et. al argues that it is essential to use non-elemental Zr for the synthesis of Zr-based MAX phases.

Interest in potential nuclear applications also motivated work on synthesis of $(Cr_{2/3}Sc_{1/3})_2AlC$ and $(Cr_{2/3}Y_{1/3})_2AlC$ *i*-MAX phases using elemental precursors [48]. However, the previous yields of the main *i*-MAX phase were insufficient for undertaking necessary bulk characterization work for service applications.

Otherwise, little work has been conducted on $(Cr_{2/3}Y_{1/3})_2AlC$ *i*-MAX phase bulk synthesis and properties. This phase was found to crystallize mainly with orthorhombic Cmcm space group with a minority phase in monoclinic C2/c space group, as reported by Lu et. al. [48]. The samples were prepared from elemental precursors and composed of 60.8 wt% $(Cr_{2/3}Y_{1/3})_2AlC$ (space group Cmcm), with impurity phases of 24.6 wt% Y_2O_3, 8.5 wt% $(Cr_{2/3}Y_{1/3})_2AlC$ (space group C2/c) and 6.1 wt% Cr_2AlC phase (space group $P6_3/mmc$), as determined by X-ray diffraction (XRD) Rietveld refinement. It is not particularly clear why orthorhombic symmetry is more favorable than monoclinic in the Cr-Y-Al-C system but Tao et. al showed energetically comparable DFT stability calculations for both symmetries [1,45].

We note in passing that substitution of Cr in out-of-plane ordered quaternary *o*-MAX phase compounds has also been realized in synthesized phases of $(Cr_{2/3}Ti_{1/3})_3AlC_2$ and $(Cr_{5/8}Ti_{3/8})_4AlC_3$ showing the possibility of tailoring of various properties [49]. Several other out-of-plane quaternary MAX phases have since been discovered [1].

To better understand the properties of the *i*-MAX phases in general and $(Cr_{2/3}Y_{1/3})_2AlC$, in particular, as well as pave the way for practical application, herein we attempted to maximize phase content of $(Cr_{2/3}Y_{1/3})_2AlC$, $(W_{2/3}Y_{1/3})_2AlC$ and $(Mo_{2/3}Y_{1/3})_2AlC$ in fully dense polycrystalline samples. This was accomplished via reactive hot-pressing, HPing, of mixtures of $Y_{2.23}Al$, elemental Al, and C combined with Cr, W, and Mo, respectively. Phase formation is confirmed using XRD; phase compositions and morphologies are investigated using Scanning Electron Microscopy (SEM), and Energy Dispersive Spectroscopy (EDS). Isothermal oxidation behavior is investigated in the range of 1000–1400 °C for 12–24 h for $(Cr_{2/3}Y_{1/3})_2AlC$ and 1300 °C for 12 h for $(Mo_{2/3}Y_{1/3})_2AlC$. Similar protocols are repeated to produce dense bulk $(W_{2/3}Y_{1/3})_2AlC$ and $(Mo_{2/3}Y_{1/3})_2AlC$ *i*-MAX phases, with varying success.

2. Materials and methods

2.1. Synthesis

Quaternary $(Cr_{2/3}Y_{1/3})_2AlC$ was synthesized by mixing reagent powders of $Y_{2.23}Al$, Cr, Al, and C (Table 1) with different starting nominal compositions (Table 2) in polyethylene jars with ZrO_2 balls for 9 h. Mixed powders were loaded in 1" diameter graphite dies

Table 2
Summary of starting compositions and hot-pressing parameters. Notes on the samples' stabilities are also listed in last column.

Sample HP#	Formula	Nominal Composition					Soak temperature and time	Sample stability status
		Basis	Cr	C	$Y_{2.23}Al$	Al		
HP1	$(Cr_{2/3}Y_{1/3})_2AlC$	wt%	43.47%	7.53%	42.23%	6.77%	1427 °C 1 h+1450 °C 3 h	Broke first into chunks and eventually into a powder.
		mol%	49.54%	37.15%	10.81%	14.88%		
HP2		wt%	40.08%	6.94%	38.94%	14.04%	1450 °C, 3 h 20 m	Broke first into chunks and eventually into a powder.
		mol%	41.78%	31.33%	9.12%	28.21%		
HP3		wt%	40.08%	6.94%	38.94%	14.04%	1500 °C, 2 h	Broke first into chunks and eventually into a powder.
		mol%	41.78%	31.33%	9.12%	28.21%		
HP4		wt%	40.72%	5.66%	39.26%	14.35%	1500 °C, 4 h	Used for oxidation tests. Sample was intact after oxidation, but disintegrated when cross-sectioned for characterization.
		mol%	41.80%	25.15%	9.05%	28.40%		
HP5		wt%	40.36%	6.29%	39.21%	14.14%	1500 °C, 4 h	Broke into big chunks after weeks in a sealed plastic bag but did not deteriorate further
		mol%	41.78%	28.20%	9.12%	28.21%		
HP6		wt%	41.00%	6.39%	39.83%	12.77%	1500 °C, 4 h	Used to steam oxidation tests, disintegrated during test.
		mol%	43.13%	29.11%	9.41%	25.89%		
HP7		wt%	41.59%	5.04%	40.41%	12.96%	1500 °C, 4 h	Broke into large sections after weeks in sealed plastic bag but did not deteriorate further
		mol%	43.13%	22.64%	9.41%	25.89%		
HP8		wt%	37.72%	5.08%	42.75%	14.44%	1500 °C, 4 h	Used for oxidation tests. Sample was intact after oxidation, but disintegrated when cross-sectioned for characterization.
		mol%	38.82%	22.65%	9.88%	28.65%		
HP9		wt%	41.59%	5.04%	40.41%	12.96%	1500 °C, 4 h	Sample broke into large sections after months in sealed plastic bag but did not deteriorate further.
		mol%	43.13%	22.64%	9.41%	25.89%		
			W	C	$Y_{2.23}Al$	Al		
HP	$(W_{2/3}Y_{1/3})_2AlC$	wt%	71.32%	2.80%	17.25%	8.64%	1550 °C, 3 h	Sample gradually deteriorated into a powder over the course of months.
		mol%	43.13%	25.88%	9.41%	25.89%		
			Mo	C	$Y_{2.23}Al$	Al		
HP	$(Mo_{2/3}Y_{1/3})_2AlC$	wt%	55.80%	4.20%	29.40%	14.10%	1550 °C, 5 h	Sample remained intact without deterioration.
		mol%	41.78%	25.07%	9.12%	28.21%		

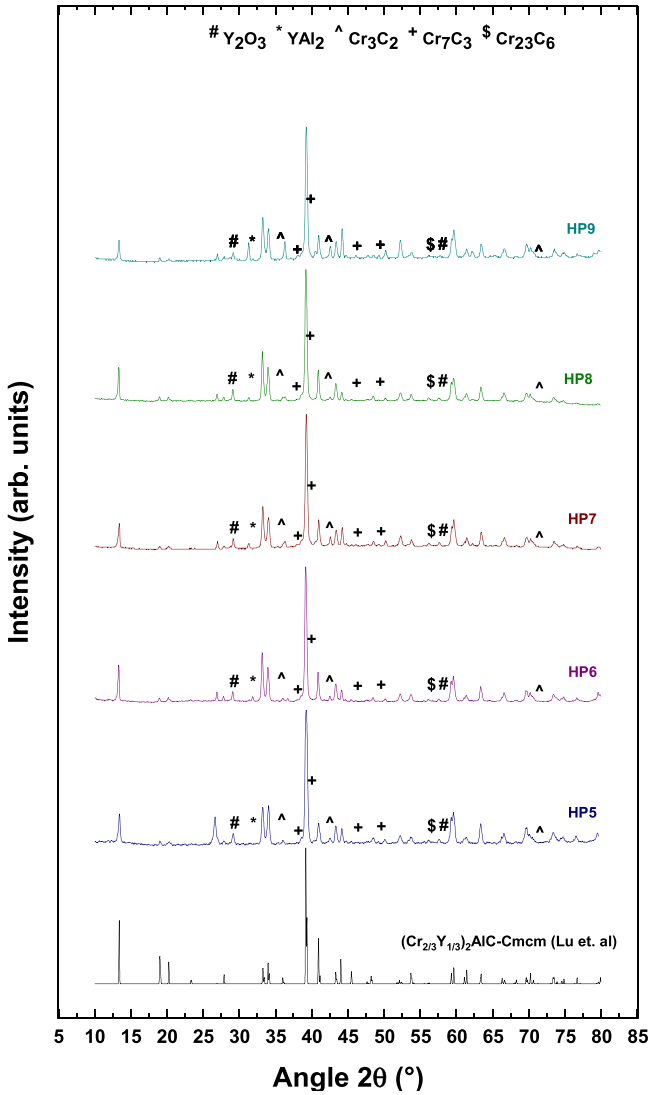

Fig. 1. XRD patterns of bulk hot pressed (HP) samples 5–9 (see Table 2). Calculated $(Cr_{2/3}Y_{1/3})_2AlC$ *i*-MAX XRD pattern (black) [48] in Cmcm space group is plotted for comparison. Labels represent # Y_2O_3, * YAl_2, ^ Cr_3C_2, + Cr_7C_3, $ $Cr_{23}C_6$, respectively.

wrapped with graphite foil and hot-pressed (HPed) to temperatures of 1450–1500 °C for 4 h with 400 °C/h ramp rate (Table 2).

In starting compositions and processing conditions attempted herein (Table 2), we use excess Al reagent. Excess Al is necessary to compensate for evaporation at high processing temperature and aluminothermic reduction of metallic powders. XRD patterns (Fig. 1) of HPed samples and Rietveld refinement (Fig. 2) are used to confirm *i*-MAX synthesis while back-scattered electron (BSE) micrographs are analyzed by image contrast analysis through ImageJ software to estimate final phase fractions. SEM micrographs used herein for phase analysis were captured at 100–300x magnification 15–25 kV at 11 mm WD, to quantify impurities and hence optimize reagent starting composition for enhanced $(Cr_{2/3}Y_{1/3})_2AlC$ phase yield (illustrated in Fig. 3).

The HPing conditions and starting reagent compositions that produced the highest $(Cr_{2/3}Y_{1/3})_2AlC$ yield were tailored for synthesis of dense bulk $(W_{2/3}Y_{1/3})_2AlC$ and $(Mo_{2/3}Y_{1/3})_2AlC$ using reagents of Table 1 and compositions of Table 2. Although Meshkian et. al [50] previously synthesized $(W_{2/3}Y_{1/3})_2AlC$ at 1450 °C, herein we chose 1550 °C for 3 h. $(Mo_{2/3}Y_{1/3})_2AlC$ was HPed herein at 1550 °C for 5 h, compared to 1500 °C for 20 h by Tao et. al [45].

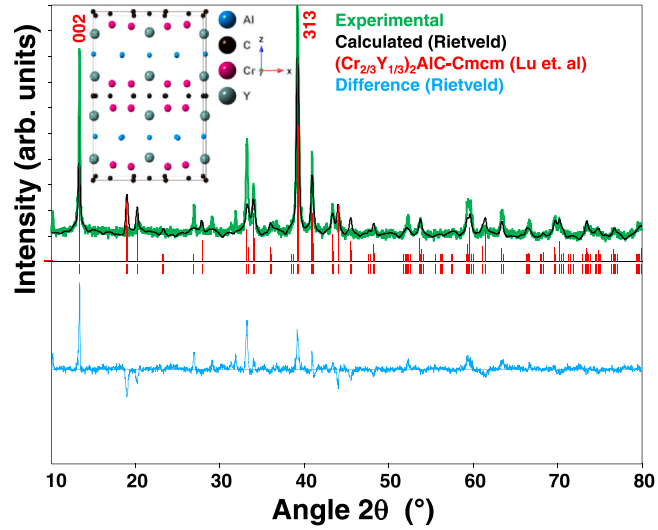

Fig. 2. Rietveld refinement of HP4 showing experimental data (green dotted curve), calculated model (black curve), Bragg reflection positions of $(Cr_{2/3}Y_{1/3})_2AlC$ (red stripes), and difference between calculated and experimental patterns (bottom magenta curve). Inset represents $(Cr_{2/3}Y_{1/3})_2AlC$ Cmcm structure with Kagomé pattern (not shown) around Al layer and "staggered" M transition metal layer in which the Y atoms are closer to the Al than the Cr atoms [48]. (For interpretation of the references to color in this figure legend, the reader is referred to the web version of this article.)

As-sintered HPed samples were polished using 240–1200 grit sized silicon-carbide paper (SiC) prior to characterization. When polished with water, the samples appeared to deteriorate in the form of pullouts. Therefore, dry polishing was used instead.

2.2. Characterization

To obtain powders, a mortar and pestle was used. XRD diffractograms of powders crushed from bulk HP samples were collected on powder diffractometers (SmartLab, Rigaku Corp., Tokyo, Japan) and (Rigaku MiniFlex 600, Japan) using 40 kV, 15–30 mA Cu-Kα radiation in a Bragg-Brentano scan mode. Scans were in the 10–80° 2θ range with a step size of 0.02° and dwell time of 1–1.8 s per step.

Rietveld refinement (Match-FullProf integrated software [51]) was carried out on XRD patterns obtained in Bragg-Brentano scanning mode in the 10–80° 2θ range and 1 s dwell time per step. A pseudo-Voigt model was used, and the refined parameters were scale factors, unit cell lattice parameters (LPs), Caglioti half-width parameters, specimen displacement, profile shape parameters and overall isotropic displacement parameters. Statistical uncertainties in estimated parameters are included in parentheses after each value. Phase distribution and impurities could not be reliably quantified solely from XRD. To estimate the impurity type and content, phase analysis was performed using a scanning electron microscope (SEM) micrographs in combination with energy-dispersive X-ray spectroscopy, EDS.

Micrographs were obtained using SEMs (Zeiss Supra 50 VP, Carl Zeiss SMT AG, Oberkochen, Germany) and (FEI/Philips XL-30 Field Emission ESEM, Hillsboro, OR, USA). Additional relative elemental compositions, phase analysis, and elemental maps were obtained with an EDS, (Oxford EDS, Oxfordshire, United Kingdom). An accelerating voltage of 15–20 kV and 15–60 s dwell times were used for the SEM micrographs and EDS measurements at an 11–15 mm working distance (WD) and a 50–60 μm aperture size.

Oxidation samples (~5 mm radius × 2 mm thick) were electro-discharge machined out of HPed bulk discs and polished down to 1200 grit using SiC paper prior to testing. The samples were weighed and then oxidized in the 1000–1400 °C temperature range under

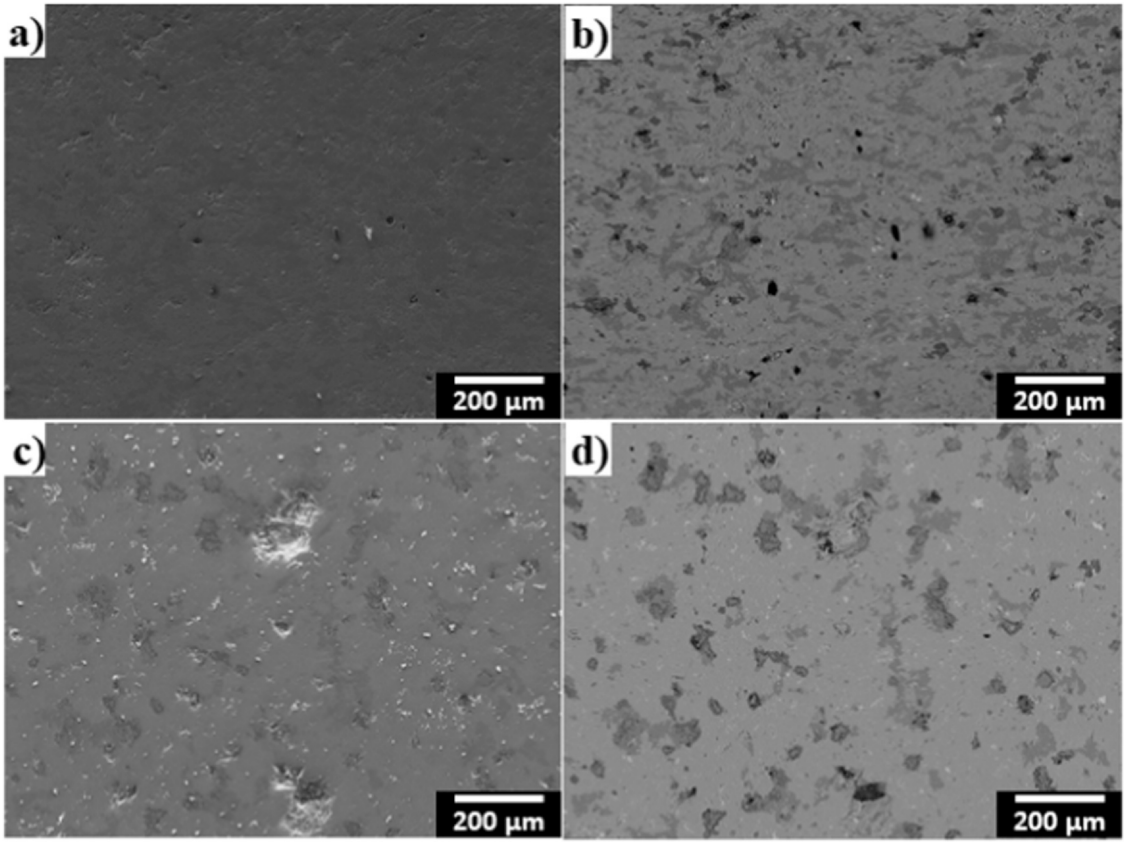

Fig. 3. Low-magnification SEM micrographs of the sample, (a) HP1 using SE, (b) same as a, but using BSE, (c) HP4 using SE, (d) same as c, but using BSE. Both samples were fully dense and HP4 had a higher *i*-MAX yield.

natural air for 12–24 h in a box furnace at a heating/cooling rate of 5 °C/min.

3. Results and discussion

3.1. Synthesis and structure of $(Cr_{2/3}Y_{1/3})_2AlC$

Powder XRD patterns of the 5 compositions HPed in this work (Table 2) are compared in Fig. 1. (A sixth is shown in Fig. 2). HP1 to 3 were significantly less single phase and are not shown. In all cases, the major peaks belong to the *i*-MAX phase in the Cmcm orthorhombic crystal structure [48]. A (110) peak at 18.99° is noted, indicating in-plane chemical order [52]. In addition, all patterns show peaks belonging to one, or more, of the following impurity phases: Y_2O_3, YAl_2 and Cr_xC_y (i.e. Cr_3C_2, Cr_7C_3, or $Cr_{23}C_6$).

Rietveld refinement was performed on XRD pattern of the HP4 sample (Fig. 2) because this run resulted in one of the highest *i*-MAX yields (see Fig. 6). The refined lattice parameters, LPs, are a = 9.3360(1) Å, b = 5.3540(2) Å and c = 13.2100 (4) Å in Cmcm space group. The χ^2 for this refinement is 5.0, the deviation from the a, b and c LPs, reported by Lu et. al [48], are −0.008%, −0.018%, −0.06%, respectively. We note in passing that in the *i*-MAX structure the Y atoms are closer to Al layer than Cr atoms, forming a staggered M layer which distinguishes *i*-MAX from traditional MAX phases (see inset in Fig. 2) [48]. The impurity phases were not quantified from XRD refinement due to; overlap between *i*-MAX and impurity peaks, relatively small quantities of some impurities and limited scan resolution. Instead image contrast analysis was carried out on BSE SEM micrographs to estimate phase fractions.

3.2. Microstructures and phase compositions

SEM micrographs and EDS maps of samples HP1 and HP4 are shown in Figs. 3–5. In all cases, the samples appear to be fully dense. The slight porosity observed is most probably due to polishing pullouts. In general, these two microstructures were comprised of five phases, confirmed by EDS. The phases are, i) the majority *i*-MAX matrix, ii) Cr_xC_y (light gray in Fig. 4a,d), iii) a Y_xAl_y intermetallic (dark gray) (Fig. 4b,e), and iv) Y_2O_3 (brightest white regions) (Fig. 4c,f). v) Al_4C_3 (not seen). No peaks corresponding to the latter phase were conclusively found in XRD patterns.

This is typical of Al_4C_3 since it tends to be poorly crystallized and/or found at the grain boundaries [53]. Initially, we hypothesized that the dark gray Al-containing regions in contact with Cr_xC_y impurity regions shown in Fig. 4d,e and Fig. 5c was the Al_4C_3 phase, however, EDS maps in Fig. 5c and d revealed this phase to be Y_xAl_y intermetallic. Attempts of identification of Al_4C_3 phase, which is hygroscopic, in the EDS were not conclusive but the sensitivity of samples to water-based polishing procedure highlights its presence as discussed by Agne et. al [53] and explains why many of the samples disintegrated to powders with time [54]. Degradation and/or subsequent disintegration had been previously attributed to volume expansion due to interaction of Al_4C_3 with moisture in SiC/Cr_2AlC [54] and Ti_2AlC-B_4C-Al [53] phase systems, respectively.

Fig. 6 summarizes the results of the image contrast analysis of BSE SEM micrographs of all the HPed runs. Not surprisingly, in all cases the *i*-MAX phase was the majority phase. It is worth noting here that our goal is to try to minimize the fractions of impurity phases. Samples with high yields; HP4, HP6 and HP8 (Fig. 6) were selected for oxidation work. HP5 and HP7 possessed high *i*-MAX

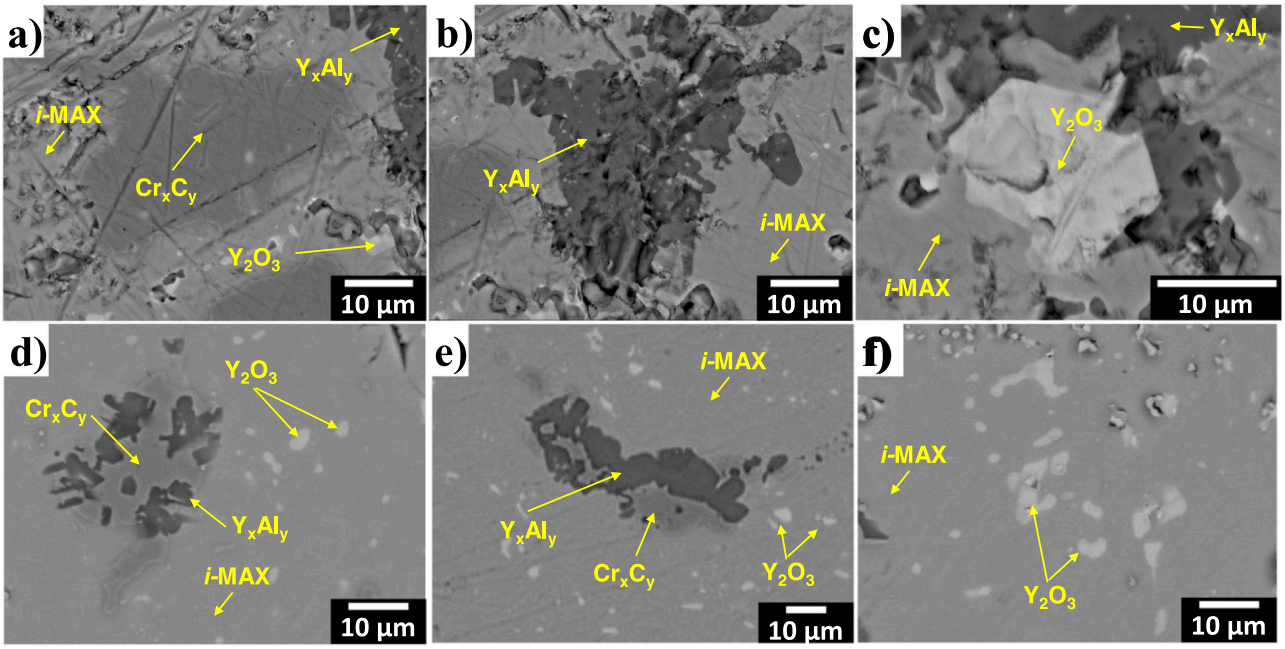

Fig. 4. BSE SEM micrographs of impurity phases in HP1 & HP4 samples surrounding *i*-MAX main phase, respectively. (a) HP1 Cr_xC_y impurity (mild gray); (b) HP1 Y_xAl_y intermetallic phase (dark gray); (c) HP1 Y_2O_3 impurities (white) (d) HP4 Cr_xC_y impurity (mild gray); (e) HP4 Y_xAl_y intermetallic phase (dark gray); (f) HP4 Y_2O_3 impurities (white).

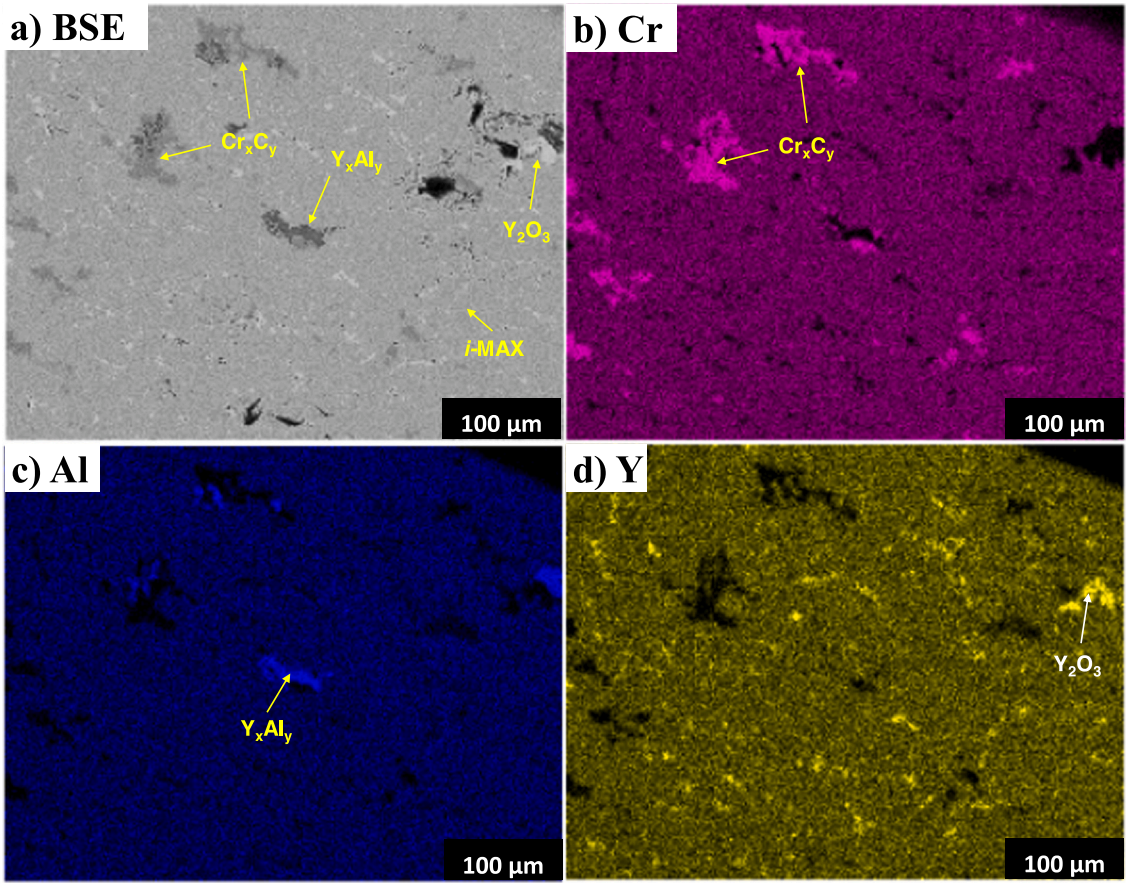

Fig. 5. SEM and EDS maps for sample HP4 showing, (a) BSE micrograph. (b) Cr map with Cr-containing regions, attributed to the Cr_xC_y phase in the 10–50 µm size range. (c) Al map showing Al-containing, Y_xAl_y in the 5–50 µm size range. (d) Y map showing bright small Y-containing regions identified as Y_2O_3 in the 10–15 µm size range.

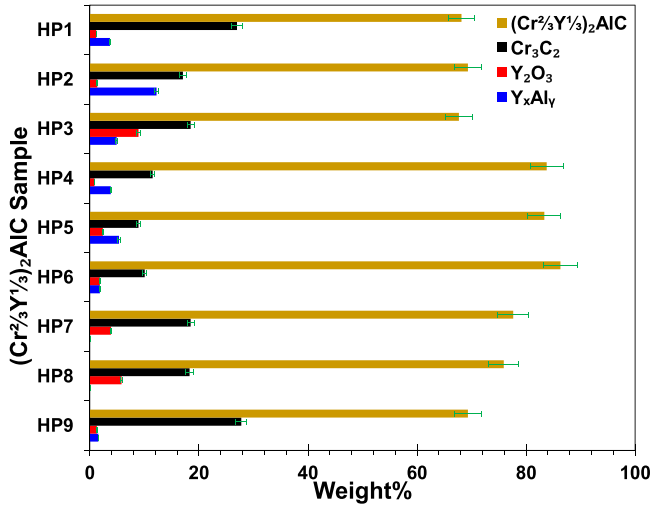

Fig. 6. Phase fractions as measured by image contrast analysis of BSE micrographs of HP runs 1–9.

yields but were not used as they had deteriorated into chunks (see Table 2) with the suspected culprit probably being Al_4C_3. The molar percentage of the *i*-MAX phase in the HP4, HP6 and HP8 samples were 84 ± 2 mol%, 86 ± 3 mol% and 76% ± 3 mol% of *i*-MAX phase, respectively.

3.3. Isothermal oxidation of $(Cr_{2/3}Y_{1/3})_2AlC$

Optical photographs of HP samples before and after oxidation are shown in Fig. 7. Oxidation at 1000 °C for 24 h, results in an adherent green oxide scale that covers the entire sample surface (Fig. 7b). The oxide layer, at this magnification, does not show evidence for spallation. After oxidation at 1200 °C for 24 h (Fig. 7c), the oxide scale appearance is not different than that after oxidation at 1000 °C but some spallation of oxide was noted. Oxidation for 12 h at 1400 °C, resulted in a relatively thick microcracked layer (Fig. 7d). Moreover, this sample was deformed compared to samples tested at lower oxidation temperatures with apparent white discoloration in the oxide scale.

By comparison of sample weight gains per unit area (ΔW/A) (Table 3) to previous work on Cr_2AlC and MoAlB [7,55], it is clear that the oxidation resistance of the *i*-MAX phase is worse within the range of oxidation conditions examined herein.

XRD patterns of the oxidized samples at 1000 °C and 1200 °C shown in Fig. 8a and b, respectively, reveal peaks belonging to $Y_3Al_2(AlO_4)_3$ (YAG), Cr_2O_3 and Y_2O_3. The small peaks at 26.30°, 32.78°, 39.24°, and 48.07° could not be identified and are marked by

Table 3
Weight gain per unit area ΔW/A in kg/m^2 of oxidized $(Cr_{2/3}Y_{1/3})_2AlC$ HP4 compared to Cr_2AlC and MoAlB samples [7,55] at similar times and temperatures.

Temperature (°C)	Time (h)	$(Cr_{2/3}Y_{1/3})_2AlC$	Cr_2AlC[7]	MoAlB[55]
1000	24	$1.5 \pm 0.1 \times 10^{-2}$	8.0×10^{-4}	Unreported
1200	24	$2.1 \pm 0.1 \times 10^{-2}$	5.3×10^{-3}	5.2×10^{-3}

"?" label. Comment notwithstanding, more work is needed to reveal the exact nature of oxide composition. At 1400 °C, the sample disintegrated after oxidation during handling and is omitted from XRD.

Polished cross-section SEM micrographs of sample oxidized at 1000 °C for 24 h (Fig. 9) indicate the presence of an outer 15 ± 4 µm thick Cr_2O_3 oxide scale layer and a 25 ± 11 µm thick inner $Y_3Al_2(AlO_4)_3$ (YAG) layer. The inner layer appears to be well adhered to the substrate, while the outermost layer seems less so. These oxide species could nominate $(Cr_{2/3}Y_{1/3})_2AlC$ *i*-MAX phase for in-situ fluorescence decay temperature sensing, and coating lifetime detection applications as in the case of Cr^{3+} doped YAG [56,57]. This comment notwithstanding, more work would be needed in that regard.

Remarkably, no evidence for formation of a continous Cr_7C_3 underlayer was found, an important distinction from oxidation in Cr_2AlC MAX phase. In the case of Cr_2AlC, a passivating Al_2O_3 forms upon oxidation with a continuous Cr_7C_3 underlayer. The Cr_7C_3 underlayer becomes problematic in the case of passivating Al_2O_3 scale breach as Al_2O_3 will not reform. It follows that the addition of Y in the *i*-MAX structure appears to disrupt binary Cr_7C_3 layer formation during isothermal oxidation.

Post-oxidation sample integrity and thick oxide scale formed during oxidation indicates that $(Cr_{2/3}Y_{1/3})_2AlC$ may be suspectible to failure in fuel cladding applications of light water nuclear reactors (LWR) in the case of loss of coolant conditions. However, at lower temperatures (i.e. 1000 °C), the oxide scale integrity is relatively adequate, the thickness of oxide formed is a limiting factor for use in fuel cladding applications. This comment notwithstanding, investigation of corrosion resistance, neutron interaction cross-section and oxidation behavior in steam or steam-H_2 environments would provide better insight into the use of $(Cr_{2/3}Y_{1/3})_2AlC$ for fuel cladding nuclear application. We note in passing that $Y_3Al_2(AlO_4)_3$ shows high dimensional and good neutron irradiation stability nominating it as a candidate for inert-matrix candidates for nuclear actinide fuels [61].

3.4. Synthesis of $(W_{2/3}Y_{1/3})_2AlC$

The XRD pattern of the HPed sample (Fig. 10) confirms the formation of the $(W_{2/3}Y_{1/3})_2AlC$ phase with (110) peak at 18.75°

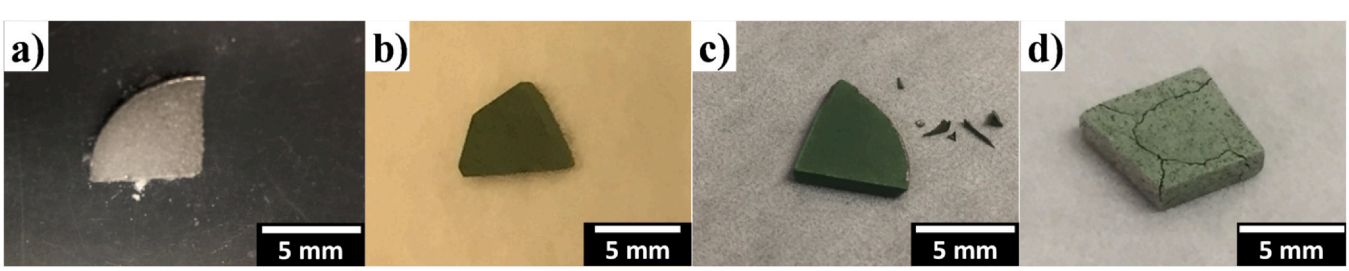

Fig. 7. Optical photographs of samples (a) HP4 before oxidation, and after oxidation at, (b) 1000 °C for 24 h, (c) 1200 °C for 24 h and (d) 1400 °C for 12 h. Sample oxidized at HP8 was used in c.

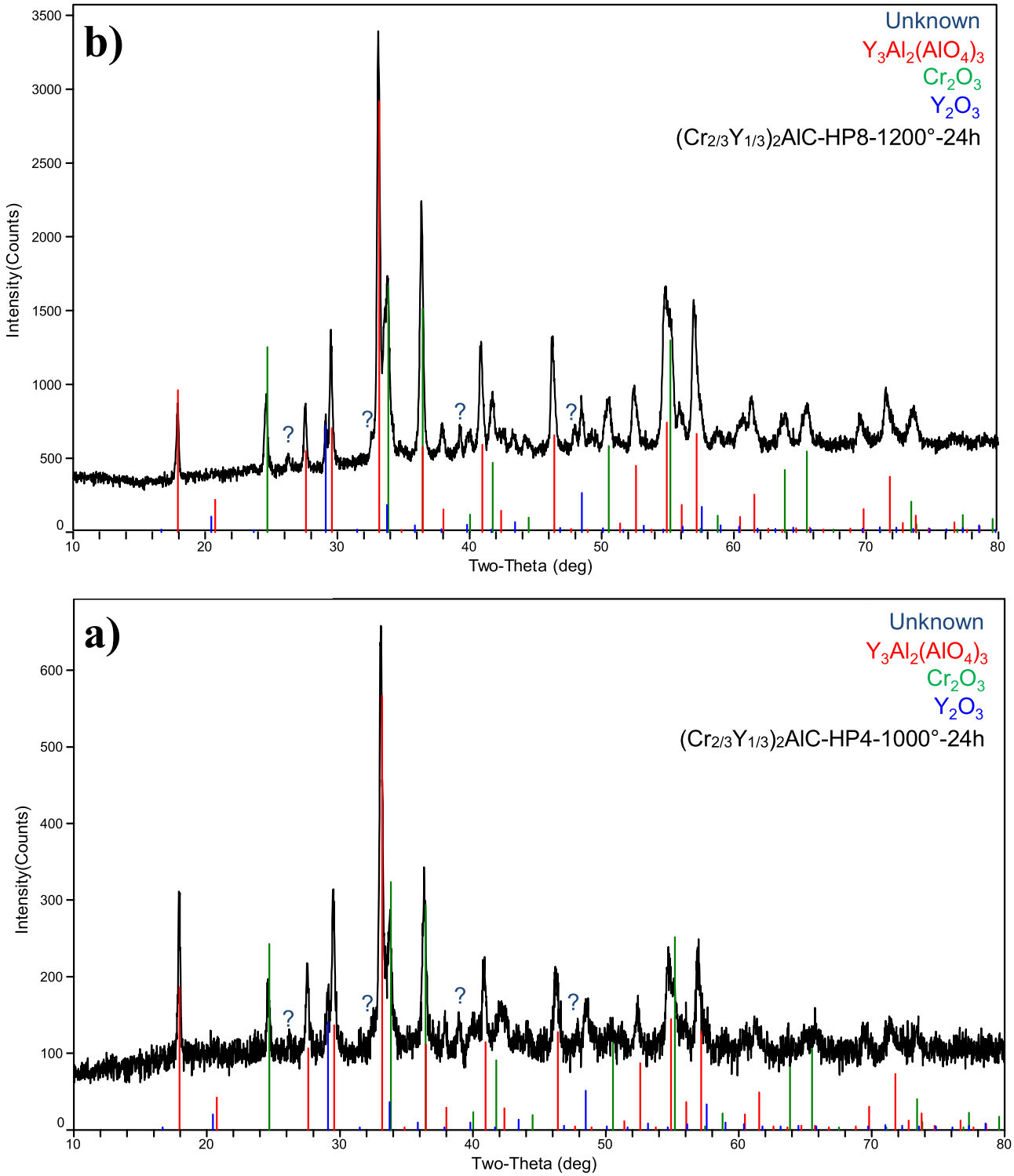

Fig. 8. XRD patterns of $(Cr_{2/3}Y_{1/3})_2AlC$-HP samples after oxidation at, a) 1000 °C for 24 h (black), b) 1200 °C for 24 h (black). Fitted phases are $Y_3Al_2(AlO_4)_3$, (red) Cr_2O_3 (green), Y_2O_3 (blue). Unknown peaks are labeled with "?".

signifying in-plane chemical order of *i*-MAX [50]. XRD patterns also contain peaks corresponding to YAl_2, and Y_2O_3, possibly from the starting reagent. It is further suggested from XRD that either some unreacted W remains, or that binary W_2C forms. *i*-MAX phase yield determined from phase fraction image contrast analysis of BSE SEM micrographs (e.g. Fig. 11) is 72 ± 3 wt% (59 ± 2 mol%). This value is higher than that obtained by Meshkian et. al (50 wt%) [62], who started with elemental reagents.

BSE SEM micrographs (Fig. 11) indicate the existence of either unreacted W or binary W_2C in the HPed sample. In future work, to

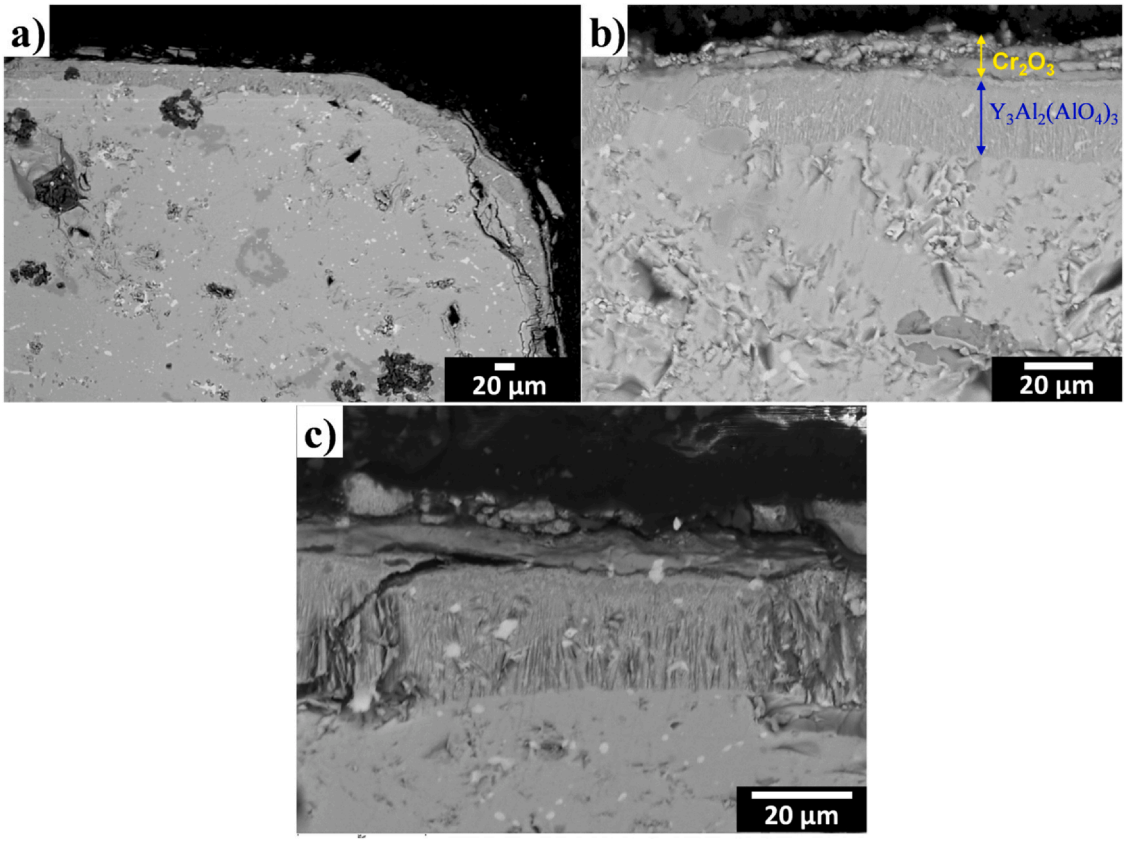

Fig. 9. BSE SEM cross-sectional micrographs of HP4 sample oxidized at 1000 °C for 24 h in air at (a) sample corner (b) lower magnification and c) at higher magnification. Cr_2O_3 outer oxide layer (15 ± 4 µm thick) covers a YAG inner layer (25 ± 11 µm).

reduce this W-based impurity, higher temperatures, longer times and/or fine-grained W powder are suggested.

3.5. Synthesis and oxidation of $(Mo_{2/3}Y_{1/3})_2AlC$

XRD of the HPed samples (Fig. 12) signify that the majority phase is the *i*-MAX with (110) peak at 18.61° indicative of in-plane chemical order of *i*-MAX, confirming phase formation in the structure previously reported by Dahlqvist et. al [46].

XRD patterns show the existence of impurity peaks from Mo_3Al and Y_2O_3. The presence of Y_2O_3 is likely due to the presence of native oxides in the starting powders.

Interestingly, phase fraction image contrast analysis of BSE SEM micrograph (Fig. 13) indicates a highly single phase structure with 91 ± 3 wt% (72 ± 2 mol%) of $(Mo_{2/3}Y_{1/3})_2AlC$ *i*-MAX phase (predominant gray phase). It is also evident from micrograph (Fig. 13b) that $Mo_{2.74}Al$ intermetallic (bright gray) phase is present, confirming XRD results. However, EDS spot analysis gives indication of substoichiometric Mo in Mo_3Al intermetallic present. There are also traces of circularly-shaped Y_2O_3 (dark gray) grains uniformly distributed in the main *i*-MAX phase.

Oxidation of $(Mo_{2/3}Y_{1/3})_2AlC$-HP1 at 1300 °C for 12 h (see Fig. 14) results in a porous white oxide with some deviation from original dimensions on the sample. Sample ΔW/A was 0.62 ± 0.02 kg/m^2, around 40 fold that of MoAlB [55]. XRD pattern (Fig. 15) of oxidized sample surface at 1300 °C for 12 h indicates that the major oxidation product is $Y_2Mo_3O_{12}$. There are two unidentified peaks at 36.44° and 57.65°. Given the poor oxidation resistance of this phase at this stage

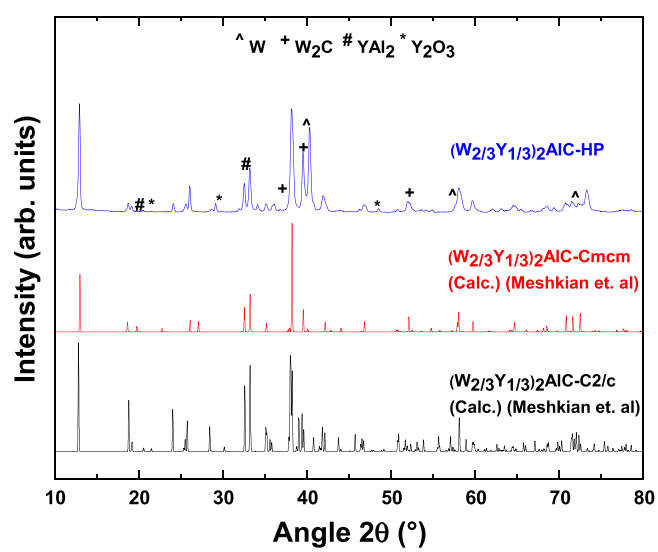

Fig. 10. XRD pattern of HPed $(W_{2/3}Y_{1/3})_2AlC$ sample (blue). Calculated *i*-MAX patterns [62] for monoclinic C2/c and orthorhombic Cmcm structures are shown in black and red, respectively.

it is an unlikely choice for high temperature applications. Whether making cleaner samples will result in better oxidation resistance is a research goal very much worth pursuing.

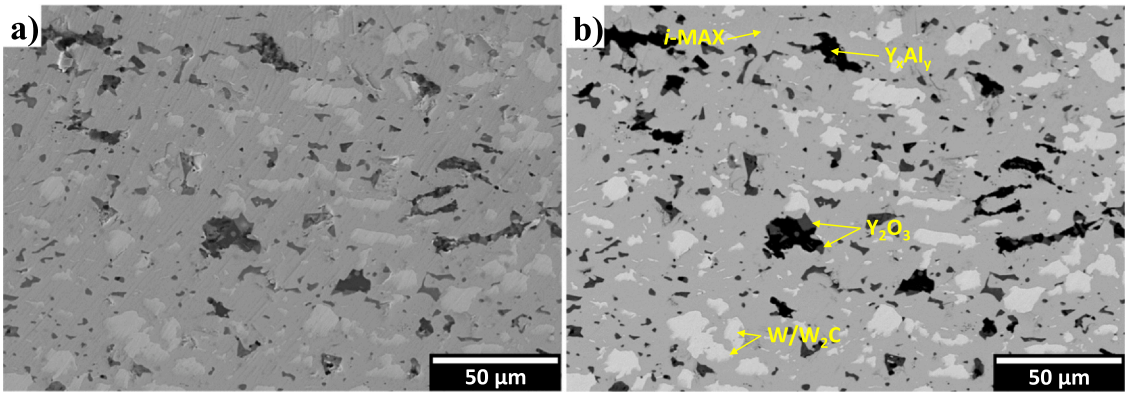

Fig. 11. SEM micrograph of HPed $(W_{2/3}Y_{1/3})_2AlC$ sample at 1550 °C for 3 h. (a) SE, and (b) BSE. Main gray phase in b is *i*-MAX, bright white phase in b is either unreacted W or W_2C, black regions are an O-containing Y_xAl_y intermetallic, dark gray regions represent Y_2O_3. Note that black regions in b are not pores.

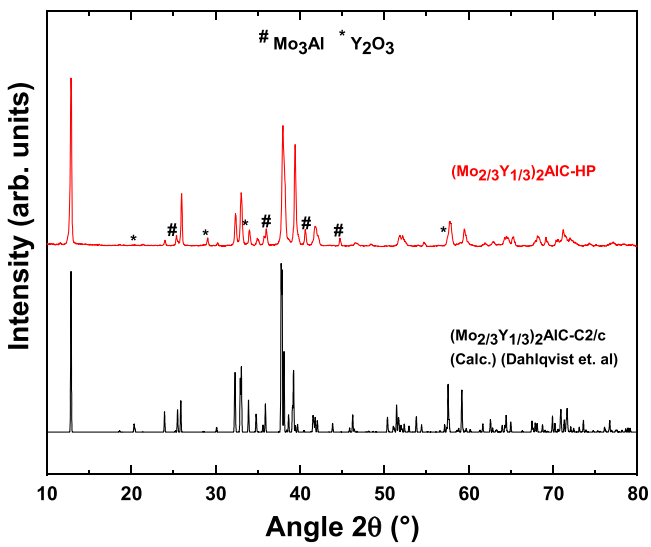

Fig. 12. X-ray diffraction (XRD) patterns of as-sintered bulk HPed $(Mo_{2/3}Y_{1/3})_2AlC$. Calculated *i*-MAX pattern [46] for monoclinic structure is shown in black. HPed XRD pattern is shown in red. Vertical dashed lines refer to peaks of: # Mo_3Al, * Y_2O_3.

4. Conclusions

Through reactive hot-pressing of $Y_{2.23}Al$, Cr, Al and C powders we produced fully dense $(Cr_{2/3}Y_{1/3})_2AlC$ polycrystalline samples with highest phase content of 85 ± 3 wt% (86 ± 3 mol%). By starting with $Y_{2.23}Al$, the content of Y_2O_3 and the undesirable ternary Cr_2AlC were reduced. Isothermal oxidation of $(Cr_{2/3}Y_{1/3})_2AlC$ produces a continuous oxide layer at 1000 °C for 24 h consisting of YAG, Cr_2O_3 and Y_2O_3. The formation of YAG could potentially nominate the use of $(Cr_{2/3}Y_{1/3})_2AlC$ for in-situ fluorescence decay temperature sensing applications. Sample weight gain at 1000 °C is around 20 times that reported Cr_2AlC. At higher temperatures of 1200–1400 °C, oxide scale integrity decreases with evidence of spallation and cracking in oxide scale.

The ternaries $(W_{2/3}Y_{1/3})_2AlC$ and $(Mo_{2/3}Y_{1/3})_2AlC$ were synthesized with yields of 72 ± 3 wt% (59 ± 2 mol%) and 91 ± 3 wt% (72 ± 2 mol%), respectively. Oxidation of $(Mo_{2/3}Y_{1/3})_2AlC$ at 1300 °C for 12 h reveals formation of a thick, porous layer of $Y_2Mo_3O_{12}$ with a weight gain was around 40 times that reported for bulk MoAlB.

CRediT authorship contribution statement

Tarek Ali ElMelegy: Conceptualization, Methodology, Validation, Formal analysis, Investigation, Data curation, Writing - original draft, Visualization **Maxim Sokol:** Methodology, Investigation, Writing - review & editing **Michel W. Barsoum:** Conceptualization, Methodology, Resources, Writing - review & editing, Supervision, Project administration, Funding acquisition.

Declaration of Competing Interest

The authors declare that they have no known competing financial interests or personal relationships that could have appeared to influence the work reported in this paper.

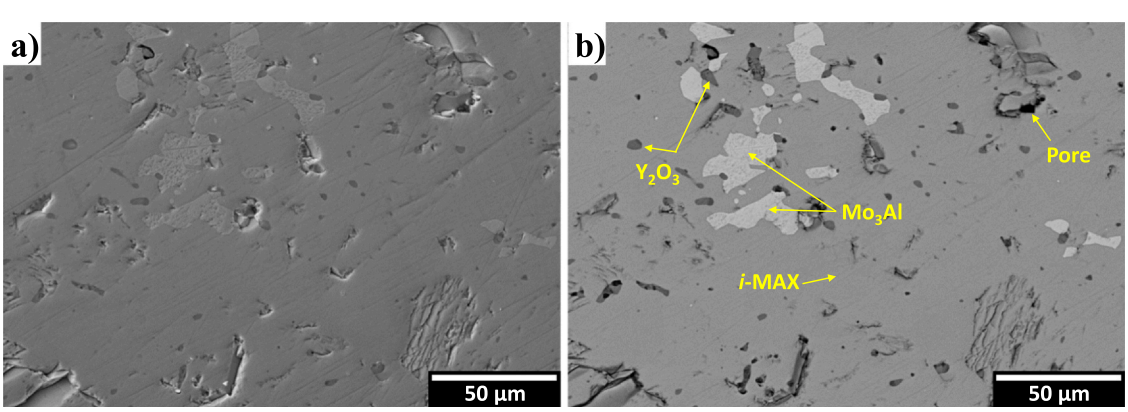

Fig. 13. SEM micrograph of $(Mo_{2/3}Y_{1/3})_2AlC$ sample HPed at 1550 °C for 5 h. (a) SE (b) BSE. Main gray phase is *i*-MAX, bright gray is a Mo_3Al ($Mo_{2.74}Al$ actual ratio) intermetallic. Small dark gray regions are Y_2O_3.

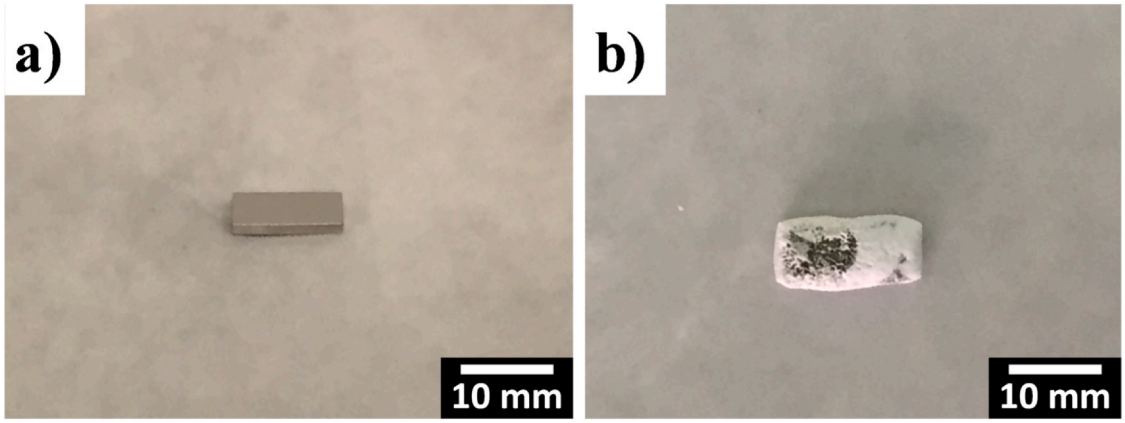

Fig. 14. Optical photographs of $(Mo_{2/3}Y_{1/3})_2AlC$ (a) before oxidation (b) after oxidation at 1300 °C for 12 h. White oxide scale formed on surface. Oxide is porous in appearance with some uncovered regions.

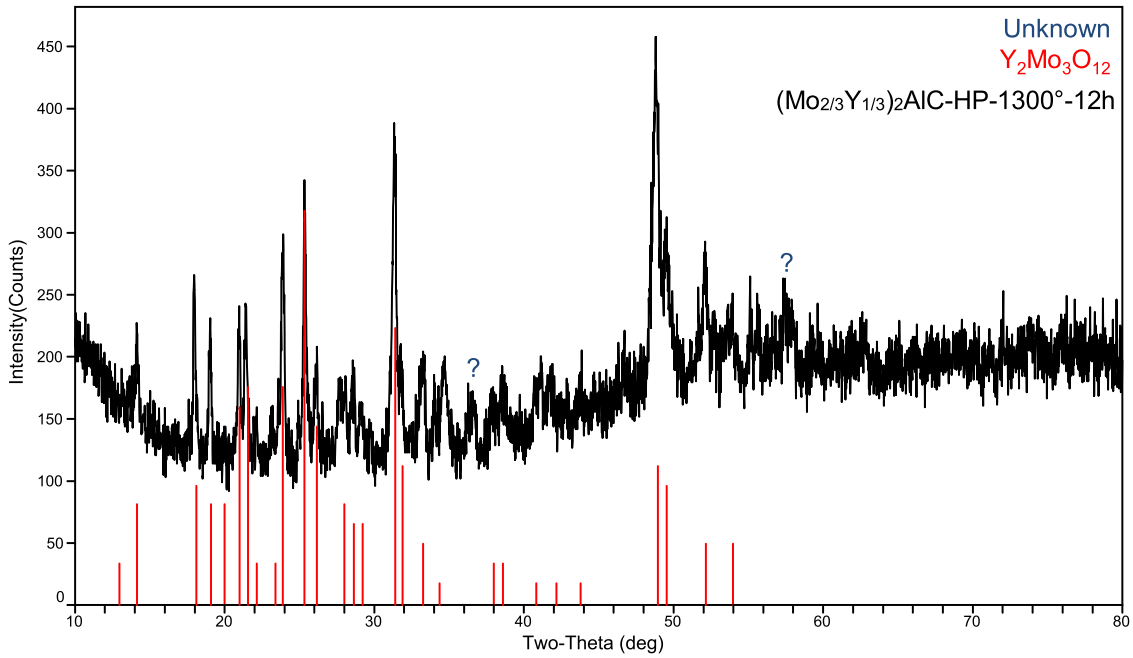

Fig. 15. XRD pattern of $(Mo_{2/3}Y_{1/3})_2AlC$-HP sample surface after oxidation (black) at 1300 °C for 12 h. Fitted phases are $Y_2Mo_3O_{12}$ (red). Unknown peaks are labeled with "?".

Acknowledgments

This work was funded by the U.S. National Science Foundation award number (DMR #1729350). The authors would like to thank Dr. Sankalp Kota for equipment training, and Hussein Badr of Drexel University for sample preparation help.

References

[1] M. Sokol, V. Natu, S. Kota, M.W. Barsoum, On the chemical diversity of the MAX phases, Trends Chem. 1 (2019) 210–223, https://doi.org/10.1016/j.trechm.2019.02.016

[2] M.W. Barsoum, MAX phases: properties of machinable ternary carbides and nitrides, 2013. doi:10.1002/9783527654581.

[3] T. Rackl, L. Eisenburger, R. Niklaus, D. Johrendt, Syntheses and physical properties of the MAX phase boride Nb_2SB and the solid solutions $Nb_2SB_xC_{1-x}$ (x=0-1), Phys. Rev. Mater. 3 (2019) 1–7, https://doi.org/10.1103/PhysRevMaterials.3.054001

[4] T. Rackl, D. Johrendt, The MAX phase borides Zr_2SB and Hf_2SB, Solid State Sci. 106 (2020) 106316, https://doi.org/10.1016/j.solidstatesciences.2020.106316

[5] J.L. Smialek, B.J. Harder, A. Garg, Oxidative durability of TBCs on Ti_2AlC MAX phase substrates, Surf. Coat. Technol. 285 (2016) 77–86, https://doi.org/10.1016/j.surfcoat.2015.11.018

[6] J.L. Smialek, S. Gray, Type II hot corrosion screening tests of a Cr_2AlC MAX phase compound, Oxid. Met. 90 (2018) 555–570, https://doi.org/10.1007/s11085-018-9857-2

[7] Z.J. Lin, M.S. Li, J.Y. Wang, Y.C. Zhou, High-temperature oxidation and hot corrosion of Cr_2AlC, Acta Mater. 55 (2007) 6182–6191, https://doi.org/10.1016/j.actamat.2007.07.024

[8] S. Li, X. Chen, Y. Zhou, G. Song, Influence of grain size on high temperature oxidation behavior of Cr_2AlC ceramics, Ceram. Int. 39 (2013) 2715–2721, https://doi.org/10.1016/j.ceramint.2012.09.039

[9] D. Eichner, A. Schlieter, C. Leyens, L. Shang, S. Shayestehaminzadeh, J.M. Schneider, Solid particle erosion behavior of nanolaminated Cr_2AlC films, Wear 402-403 (2018) 187–195, https://doi.org/10.1016/j.wear.2018.02.014

[10] J. Gonzalez-Julian, T. Go, D.E. Mack, R. Vaßen, Environmental resistance of Cr_2AlC MAX phase under thermal gradient loading using a burner rig, J. Am. Ceram. Soc. 101 (2018) 1841–1846, https://doi.org/10.1111/jace.15425

[11] D. Horlait, S. Grasso, N. Al Nasiri, P.A. Burr, W.E. Lee, Synthesis and oxidation testing of MAX phase composites in the Cr-Ti-Al-C quaternary system, J. Am. Ceram. Soc. 99 (2016) 682–690, https://doi.org/10.1111/jace.13962

[12] J.L. Smialek, J.A. Nesbitt, T.P. Gabb, A. Garg, R.A. Miller, Hot corrosion and low cycle fatigue of a Cr_2AlC-coated superalloy, Mater. Sci. Eng. A 711 (2018) 119–129, https://doi.org/10.1016/j.msea.2017.10.098

[13] D.J. Tallman, B. Anasori, M.W. Barsoum, A critical review of the oxidation of Ti_2AlC, Ti_3AlC_2 and Cr_2AlC in air, Mater. Res. Lett. 1 (2013) 115–125, https://doi.org/10.1080/21663831.2013.806364

[14] W. Tian, P. Wang, Y. Kan, G. Zhang, Oxidation behavior of Cr2AlC ceramics at 1,100 and 1,250°C, J. Mater. Sci. 43 (2008) 2785–2791, https://doi.org/10.1007/s10853-008-2516-2

[15] M. Sokol, J. Yang, H. Keshavan, M.W. Barsoum, Bonding and oxidation protection of Ti_2AlC and Cr_2AlC for a Ni-based superalloy, J. Eur. Ceram. Soc. 39 (2019) 878–882, https://doi.org/10.1016/j.jeurceramsoc.2018.10.019

[16] D.E. Hajas, M. Baben, B. Hallstedt, R. Iskandar, J. Mayer, J.M. Schneider, Oxidation of Cr_2AlC coatings in the temperature range of 1230 to 1410°C, Surf. Coat. Technol. 206 (2011) 591–598, https://doi.org/10.1016/j.surfcoat.2011.03.086

[17] D.B. Lee, T.D. Nguyen, S.W. Park, Long-time oxidation of Cr_2AlC between 700 and 1,000 °C in air, Oxid. Met. 77 (2012) 275–287, https://doi.org/10.1007/s11085-012-9285-7

[18] H.J. Yang, Y.T. Pei, J.T.M. De Hosson, Oxide-scale growth on Cr_2AlC ceramic and its consequence for self-healing, Scr. Mater. 69 (2013) 203–206, https://doi.org/10.1016/j.scriptamat.2013.04.013

[19] D.B. Lee, T.D. Nguyen, Cyclic oxidation of Cr_2AlC between 1000 and 1300°C in air, J. Alloy. Compd. 464 (2008) 434–439, https://doi.org/10.1016/j.jallcom.2007.10.018

[20] M. Ougier, A. Michau, F. Lomello, F. Schuster, H. Maskrot, M.L. Schlegel, High-temperature oxidation behavior of HiPIMS as-deposited Cr–Al–C and annealed Cr_2AlC coatings on Zr-based alloy, J. Nucl. Mater. 528 (2020) 151855, https://doi.org/10.1016/j.jnucmat.2019.151855

[21] J. Ward, D. Bowden, E. Prestat, S. Holdsworth, D. Stewart, M.W. Barsoum, M. Preuss, P. Frankel, Corrosion performance of Ti_3SiC_2, Ti_3AlC_2, Ti_2AlC and Cr_2AlC MAX phases in simulated primary water conditions, Corros. Sci. 139 (2018) 444–453, https://doi.org/10.1016/j.corsci.2018.04.034

[22] Z.G. Yang, P.Y. Hou, Wrinkling behavior of alumina scales formed during isothermal oxidation of Fe-Al binary alloys, Mater. Sci. Eng. A 391 (2005) 1–9, https://doi.org/10.1016/j.msea.2004.05.016

[23] V.K. Tolpygo, D.R. Clarke, Wrinkling of α-alumina films grown by oxidation – II. Oxide separation and failure, Acta Mater. 46 (1998) 5167–5174, https://doi.org/10.1016/S1359-6454(98)00134-7

[24] V.K. Tolpygo, D.R. Clarke, Wrinkling of α-alumina films grown by thermal oxidation – I. Quantitative studies on single crystals of Fe-Cr-Al alloy, Acta Mater. 46 (1998) 5153–5166, https://doi.org/10.1016/S1359-6454(98)00133-5

[25] S. Kota, E. Zapata-Solvas, Y. Chen, M. Radovic, W.E. Lee, M.W. Barsoum, Isothermal and cyclic oxidation of MoAlB in air from 1100°C to 1400°C, J. Electrochem. Soc. 164 (2017) C930–C938, https://doi.org/10.1149/2.1891713jes

[26] Z. Suo, Wrinkling of the oxide scale on an aluminum-containing alloy at high temperatures, J. Mech. Phys. Solids 43 (1995) 829–846, https://doi.org/10.1016/0022-5096(95)00014-A

[27] Z. Liu, W. Gao, Y. He, Modeling of oxidation kinetics of Y-doped Fe-Cr-Al alloys, Oxid. Met. 53 (2000) 341–350, https://doi.org/10.1023/A:1004545421739

[28] D. Naumenko, B. Gleeson, E. Wessel, L. Singheiser, W.J. Quadakkers, Correlation between the microstructure, growth mechanism, and growth kinetics of alumina scales on a FeCrAlY alloy, Metall. Mater. Trans. A Phys. Metall. Mater. Sci. 38 A (2007) 2974–2983, https://doi.org/10.1007/s11661-007-9342-z

[29] W.J. Quadakkers, D. Naumenko, E. Wessel, V. Kochubey, L. Singheiser, Growth rates of alumina scales on Fe-Cr-Al alloys, Oxid. Met. 61 (2004) 17–37, https://doi.org/10.1023/b:oxid.0000016274.78642.ae

[30] D.J. Young, D. Naumenko, L. Niewolak, E. Wessel, L. Singheiser, W.J. Quadakkers, Oxidation kinetics of Y-doped FeCrAl-alloys in low and high pO_2 gases, Mater. Corros. 61 (2010) 838–844, https://doi.org/10.1002/maco.200905432

[31] J.L. Smialek, Unusual oxidative limitations for Al-MAX phases. NASA/TM—2017–219444, 2017. ⟨http://www.sti.nasa.gov/ and http://ntrs.nasa.gov/⟩.

[32] V.K. Tolpygo, H.J. Grabke, The effect of impurities on the alumina scale growth: an alternative view, Scr. Mater. 38 (1997) 123–129, https://doi.org/10.1016/S1359-6462(97)00451-X

[33] R. Cueff, H. Buscail, E. Caudron, C. Issartel, F. Riffard, Oxidation behaviour of Kanthal APM and Kanthal AF at 1173 K: effect of yttrium alloying addition, Surf. Eng. 19 (2003) 58–64, https://doi.org/10.1179/026708403225002469

[34] B.A. Pint, Experimental observations in support of the dynamic-segregation theory to explain the reactive-element effect, Oxid. Met. 45 (1996) 1–37, https://doi.org/10.1007/BF01046818

[35] B.A. Pint, J.R. Martin, L.W. Hobbs, 18O/SIMS characterization of the growth mechanism of doped and undoped α-Al_2O_3, Oxid. Met. 39 (1993) 167–195, https://doi.org/10.1007/BF00665610

[36] C. Mennicke, E. Schumann, M. Rühle, R.J. Hussey, G.I. Sproule, M.J. Graham, The effect of yttrium on the growth process and microstructure of α-Al_2O_3 on FeCrAl, Oxid. Met. 49 (1998) 455–466, https://doi.org/10.1023/A:1018803113093

[37] F.A. Golightly, F.H. Stott, G.C. Wood, The influence of yttrium additions on the oxide-scale adhesion to an iron-chromium-aluminum alloy, Oxid. Met. 10 (1976) 163–187, https://doi.org/10.1007/BF00612158

[38] K.A. Unocic, Y. Yamamoto, B.A. Pint, Effect of Al and Cr content on air and steam oxidation of FeCrAl alloys and commercial APMT alloy, Oxid. Met. 87 (2017) 431–441, https://doi.org/10.1007/s11085-017-9745-1

[39] N. Mortazavi, C. Geers, M. Esmaily, V. Babic, M. Sattari, K. Lindgren, P. Malmberg, B. Jönsson, M. Halvarsson, J.E. Svensson, I. Panas, L.G. Johansson, Interplay of water and reactive elements in oxidation of alumina-forming alloys, Nat. Mater. 17 (2018) 610–617, https://doi.org/10.1038/s41563-018-0105-6

[40] C. Tang, A. Jianu, M. Steinbrueck, M. Grosse, A. Weisenburger, H.J. Seifert, Influence of composition and heating schedules on compatibility of FeCrAl alloys with high-temperature steam, J. Nucl. Mater. 511 (2018) 496–507, https://doi.org/10.1016/j.jnucmat.2018.09.026

[41] Z. Yang, J. Pan, Z. Wang, Y. Wu, G. Jia, J. Li, X. Xiao, New insights into the mechanism of yttrium changing high-temperature oxide growth of Fe-13Cr–6Al–2Mo–0.5Nb alloy for fuel cladding, Corros. Sci. 172 (2020) 108728, https://doi.org/10.1016/j.corsci.2020.108728

[42] O. Berger, R. Boucher, M. Ruhnow, Part II. Oxidation of yttrium doped Cr_2AlC films in temperature range between 700 and 1200°C, Surf. Eng. 31 (2015) 386–396, https://doi.org/10.1179/1743294414Y.0000000418

[43] O. Berger, R. Boucher, Crack healing in Y-doped Cr_2AlC-MAX phase coatings, Surf. Eng. 33 (2017) 192–203, https://doi.org/10.1080/02670844.2016.1201366

[44] R. Boucher, O. Berger, Magnetic model of oxidation process of Y containing Cr–Al–C films, Surf. Eng. 34 (2018) 6–13, https://doi.org/10.1179/1743294415Y.0000000002

[45] Q. Tao, M. Dahlqvist, J. Lu, S. Kota, R. Meshkian, J. Halim, J. Palisaitis, L. Hultman, M.W. Barsoum, P.O.Å. Persson, J. Rosen, Two-dimensional $Mo_{1.33}C$ MXene with divacancy ordering prepared from parent 3D laminate with in-plane chemical ordering, Nat. Commun. 8 (2017) 1–7, https://doi.org/10.1038/ncomms14949

[46] M. Dahlqvist, J. Lu, R. Meshkian, Q. Tao, L. Hultman, J. Rosen, Prediction and synthesis of a family of atomic laminate phases with Kagomé-like and in-plane chemical ordering, Sci. Adv. 3 (2017) e1700642, https://doi.org/10.1126/sciadv.1700642

[47] L. Chen, M. Dahlqvist, T. Lapauw, B. Tunca, F. Wang, J. Lu, R. Meshkian, K. Lambrinou, B. Blanpain, J. Vleugels, J. Rosen, Theoretical prediction and synthesis of $(Cr_{2/3}Zr_{1/3})_2AlC$ i-MAX phase, Inorg. Chem. 57 (2018) 6237–6244, https://doi.org/10.1021/acs.inorgchem.8b00021

[48] J. Lu, A. Thore, R. Meshkian, Q. Tao, L. Hultman, J. Rosen, Theoretical and experimental exploration of a novel in-plane chemically ordered $(Cr_{2/3}M_{1/3})_2AlC$ i-MAX phase with M = Sc and y, Cryst. Growth Des. 17 (2017) 5704–5711, https://doi.org/10.1021/acs.cgd.7b00642

[49] H.H. Qarra, K.M. Knowles, M.E. Vickers, S. Akhmadaliev, K. Lambrinou, Heavy ion irradiation damage in Zr_2AlC MAX phase, J. Nucl. Mater. 523 (2019) 1–9, https://doi.org/10.1016/j.jnucmat.2019.05.034

[50] R. Meshkian, M. Dahlqvist, J. Lu, B. Wickman, J. Halim, J. Thörnberg, Q. Tao, S. Li, S. Intikhab, J. Snyder, M.W. Barsoum, M. Yildizhan, J. Palisaitis, L. Hultman, P.O.Å. Persson, J. Rosen, W-based atomic laminates and their 2D derivative $W_{1.33}C$ MXene with vacancy ordering, Adv. Mater. 30 (2018) 1706409, https://doi.org/10.1002/adma.201706409

[51] H. Putz, K. Brandenburg, M. GbR, Phase identification from powder diffraction, crystal impact. Kreuzherrenstr. 102, 53227 Bonn, Germany, (2018).

[52] M. Dahlqvist, A. Petruhins, J. Lu, L. Hultman, J. Rosen, Origin of chemically ordered atomic laminates (i-MAX): expanding the elemental space by a theoretical/experimental approach, ACS Nano 12 (2018) 7761–7770, https://doi.org/10.1021/acsnano.8b01774

[53] M.T. Agne, B. Anasori, M.W. Barsoum, Reactions between Ti_2AlC, B4C, and Al and phase equilibria at 1000 °C in the Al-Ti-B-C quaternary system, J. Phase Equilibr. Diffus. 36 (2015) 169–182, https://doi.org/10.1007/s11669-015-0371-9

[54] H.L. Li, S.B. Li, X.D. Chen, Y. Zhou, Spontaneous pulverisation of Al_4C3 containing MAX bulk ceramics at room temperature, Adv. Appl. Ceram. 113 (2014) 184–188, https://doi.org/10.1179/1743676114Y.0000000142

[55] S. Kota, E. Zapata-Solvas, Y. Chen, M. Radovic, W.E. Lee, M.W. Barsoum, Isothermal and cyclic oxidation of MoAlB in air from 1100°C to 1400°C, J. Electrochem. Soc. 164 (2017) C930–C938, https://doi.org/10.1149/2.1891713jes

[56] H. Aizawa, T. Katsumata, Y. Kiyokawa, T. Nishikawa, T. Sasagawa, S. Komuro, T. Morikawa, H. Ishizawa, E. Toba, Evaluation of Cr-doped yttrium aluminum garnet crystals for hybrid fiber-optic thermometer application, Meas. J. Int. Meas. Confed. 39 (2006) 147–152, https://doi.org/10.1016/j.measurement.2005.10.004

[57] L. Ye, J. Zhang, Y. Shi, Growth and characteristics of Cr^{3+}: YAG crystal fiber for fluorescence decay temperature sensor, Rev. Sci. Instrum. 77 (2006) 054901, https://doi.org/10.1063/1.2200889

[61] R.J. Konings, K. Bakker, J. Boshoven, R. Conrad, H. Hein, The influence of neutron irradiation on the microstructure of Al_2O_3, $MgAl_2O_4$, $Y_3Al_5O_{12}$ and CeO_2, J. Nucl. Mater. 254 (1998) 135–142, https://doi.org/10.1016/S0022-3115(97)00355-3

[62] R. Meshkian, M. Dahlqvist, J. Lu, B. Wickman, J. Halim, J. Thörnberg, Q. Tao, S. Li, S. Intikhab, J. Snyder, M.W. Barsoum, M. Yildizhan, J. Palisaitis, L. Hultman, P.O.Å. Persson, J. Rosen, W-based atomic laminates and their 2D derivative W1.33C MXene with vacancy ordering, Adv. Mater. 30 (2018) 1706409, https://doi.org/10.1002/adma.201706409